

# 2D Triangle Splatting for Direct Differentiable Mesh Training

Kaifeng Sheng\*, Zheng Zhou\*, Yingliang Peng, Qianwei Wang<sup>†</sup>  
AMAP

{shengkaifeng.skf, zhouzheng.zhou, yingliang.pyl, qianwei.wang}@alibaba-inc.com

## Abstract

*Differentiable rendering with 3D Gaussian primitives has emerged as a powerful method for reconstructing high-fidelity 3D scenes from multi-view images. While it offers improvements over NeRF-based methods, this representation still encounters challenges with rendering speed and advanced rendering effects, such as relighting and shadow rendering, compared to mesh-based models. In this paper, we propose 2D Triangle Splatting (2DTS), a novel method that replaces 3D Gaussian primitives with 2D triangle facelets. This representation naturally forms a discrete mesh-like structure while retaining the benefits of continuous volumetric modeling. By incorporating a compactness parameter into the triangle primitives, we enable direct training of photorealistic meshes. Our experimental results demonstrate that our triangle-based method, in its vanilla version (without compactness tuning), achieves higher fidelity compared to state-of-the-art Gaussian-based methods. Furthermore, our approach produces reconstructed meshes with superior visual quality compared to existing mesh reconstruction methods. Please visit our project page at <https://gaoderender.github.io/triangle-splatting>.*

## 1. Introduction

Reconstructing consistent 3D geometry and synthesizing novel views from multiview images has been a long-standing challenge in computer vision. Traditional Multi-View Stereo (MVS) pipelines [27] generate point clouds by identifying correspondences between images and then reconstructing textured meshes from these point clouds. However, the accuracy of these methods is limited by the quality of detected correspondences and suffers from issues with non-Lambertian surfaces and textureless regions. They also tend to produce over-smoothed surfaces and struggle to represent thin structures due to limitations in the triangulation process.

The field has advanced significantly with the recent application of differentiable rendering and back-propagation-based optimization methods. Neural radiance fields (NeRF) [24] represent geometry with a continuous function approximated by neural networks, improving upon traditional mesh-based methods in the visual quality of synthesized novel views. However, their applications are limited by high computational costs and the lack of explicit geometry representation. 3D Gaussian splatting (3DGS) [17] addresses these limitations by representing geometry with 3D Gaussian primitives and implementing an efficient splatting method for differentiable rendering. 3DGS has proven more efficient than NeRF-based methods and can potentially achieve real-time rendering [22]. However, the geometry from 3DGS still deviates from the actual scene geometry due to the diffused nature of Gaussian kernels. Recent works have improved 3DGS representation by rendering more accurate depth [3, 34] or replacing 3D Gaussians with primitives that have better geometric properties, such as 2D Gaussian plates [15] or 3D convexes [14].

Despite these improvements, splatting-based models are far less frequently used than mesh models in real-world applications. One key reason is that splatting-based models require specially designed rendering pipelines and remain incompatible with existing rendering engines. Although there have been recent attempts [10], achieving advanced rendering effects, such as relighting and shadow rendering, with splatting-based models remains challenging. The computationally intensive depth sorting and alpha-blending operations used in splatting-based methods also hinder their deployment on resource-constrained devices. To extract triangle meshes from splatting-based models, a post-processing step using Truncated Signed Distance Function (TSDF) [26, 36] is typically required. This post-processing step is not differentially optimized and may introduce artifacts in the final mesh. It also reduces the Lagrangian representation of Gaussian primitives to a voxel-based Eulerian representation, creating a trade-off between computational complexity and geometric fidelity [11]. Compared to their original representation, meshes extracted from Gaussian-based methods are either too large or too coarse to efficiently rep-

\*Equal contribution.

<sup>†</sup>Corresponding author.

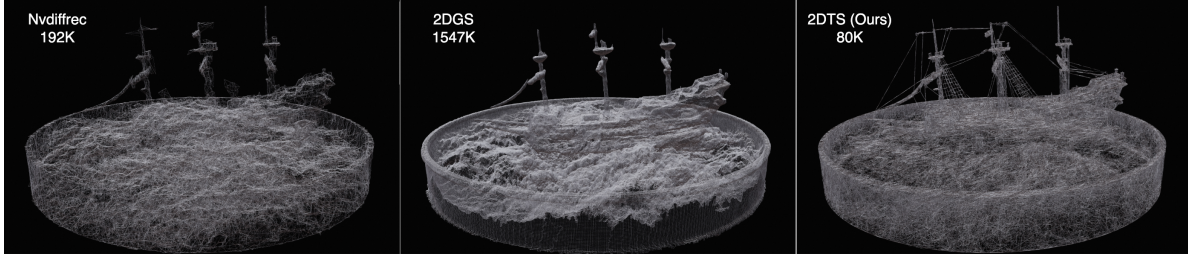


Figure 1. **2D Triangle Splatting for Mesh Reconstruction.** A wireframe comparison of the reconstructed mesh by our proposed 2D Triangle Splatting method with 2DGS [15] and Nvdiffrac [25]. Our method reconstruct meshes with higher geometric accuracy and visual quality with fewer faces. Note that the thin structures in the scene are better preserved by our method.

resent different levels of detail in the scene. A method that combines the portability and efficiency of mesh-based models with the visual fidelity of radiance-field-based models is highly desirable.

In this work, we propose a novel approach that replaces the Gaussian primitives in 3DGS with 2D triangle facelets. These facelets feature spatially varying opacity based on the barycentric coordinates of each point on the triangle plane, preserving differentiability with respect to vertex locations throughout the rendering process. We demonstrate that by replacing 3D Gaussians with 2D triangles, we achieve comparable or improved visual quality compared to state-of-the-art Gaussian-based methods [17, 33]. Figure 1 shows a comparison between 2D Gaussian splatting [15], Nvdiffrac [25] and our proposed 2D Triangle Splatting method.

To bridge the gap between diffusive facelet representation and solid mesh representation, we introduce a compactness parameter inspired by Generalized Exponential Splatting (GES) [12] to the triangle primitives. This parameter controls the sharpness of triangle facelet edges by replacing the exponential decay function of 3DGS with a Generalized Exponential Function (GEF). Rather than learning the compactness parameter, we employ a training schedule that gradually increases facelet compactness during training, yielding a solid mesh representation at conclusion. Because our entire training process is end-to-end without requiring post-processing, our method produces meshes with higher visual quality than previous approaches, as demonstrated in our experiments. Although the meshes generated by our method are not watertight, they perform well in downstream tasks such as relighting and shadow rendering. Our approach thus offers an attractive solution for rendering-focused applications such as 3D map reconstruction and virtual reality.

## 2. Related Work

The field of 3D reconstruction and novel view synthesis (NVS) has rapidly evolved, particularly since the introduction of Neural Radiance Fields (NeRF) [24]. In this section,

we review the most relevant works in the field, focusing on mesh and texture extraction methods. All methods discussed below share the same input data: a set of multi-view images and camera poses.

### 2.1. Multi-View Stereo

Multi-view stereo (MVS) encompasses techniques that use stereo correspondences to reconstruct 3D geometry from multiple images [8]. This approach has been extensively studied in computer vision for decades. MVS methods can be broadly categorized into depth-map-based methods and volumetric-based methods. Depth-map-based methods [9, 27] estimate depth maps for each view and then fuse them into a coherent 3D model. Volumetric methods [16, 19] represent the scene as a volumetric grid and iteratively refine it to match observed images. While traditional MVS methods rely on handcrafted features and matching metrics, recent approaches leverage deep learning to improve depth estimation accuracy and robustness [4, 31]. Despite their success, MVS methods often struggle with textureless regions, reflective surfaces, and thin structures, resulting in incomplete or noisy reconstructions.

### 2.2. Neural Radiance Field

Mildenhall *et al.* [24] introduced Neural Radiance Fields (NeRF) as a novel differentiable representation for 3D scenes. NeRF represents scenes as continuous functions mapping 3D coordinates to radiance and volume density values, using neural networks as function approximators. Barron *et al.* [1, 2] enhanced NeRF by introducing multi-scale representation and hierarchical sampling strategies. They extended the method to unbounded scenes and reduced artifacts common in NeRF-based methods. To extract meshes from NeRF representations, the marching cubes algorithm [23] is typically applied to density fields evaluated on voxel grids. However, due to network expressivity limitations and the fact that the model is not directly optimized for geometry capture, extracted meshes often appear coarse and lack fine details.

## 2.3. Splatting-Based Methods

Splatting-based methods represent scenes as sets of geometric primitives and employ a splatting technique introduced by Kerbl *et al.* [17] to render scenes efficiently and differentially. The original work [17] used 3D Gaussian primitives, while Huang *et al.* [15] proposed 2D Gaussian plates to enhance geometric accuracy. Zhang *et al.* [34] and Chen *et al.* [3] improved depth rendering by implementing more accurate depth calculation methods. Hamdi *et al.* [12] introduced GES to increase Gaussian kernel expressiveness while reducing the number of primitives needed for scene representation. Held *et al.* [14] further increased expressiveness by employing 3D convexes as primitives. Other works [32, 35] combine Gaussian Splatting with Signed Distance Functions (SDFs), jointly optimizing both representations while maintaining consistency between them. These approaches constrain Gaussian primitives to lie on object surfaces within the scene.

For mesh extraction from splatting-based representations, the standard approach involves rendering depth maps for each view and fusing them using TSDF methods [26, 36]. Since TSDF methods are grid-based, the resulting meshes cannot express varying levels of detail as effectively as the original primitive representation.

## 2.4. Gradient-based Mesh Optimization

Recent research has explored gradient-based optimization to directly reconstruct mesh and texture representations from multi-view images. DMTet [28] represents scenes as SDFs evaluated on deformable tetrahedral grids and implements differentiable marching tetrahedra for mesh extraction. FlexiCube [29] utilizes cubic grids and Dual Marching Cubes for mesh extraction, introducing additional parameters to enhance mesh representation flexibility. While these approaches utilize 3D supervision, Munkberg *et al.* [25] built upon DMTet and employed deferred shading [20] to enable joint mesh and texture optimization with 2D image supervision. MobileNeRF [5] also optimizes colored meshes using differentiable rendering, with the mesh vertices initialized as a regular Euclidean lattice and locally optimized during training. The mesh color is parameterized by a MLP and rendered using deferred shading. However, being grid-based, these methods are constrained by grid resolution and cannot efficiently represent different levels of detail in a large-scale scene.

## 2.5. Concurrent Work

Differentiable rendering and 3D reconstruction remain active research areas with continuously emerging methods. Here, we highlight recent works closely related to our approach.

Guo *et al.* [11] proposed modeling 3D shapes using deformable volumetric tetrahedral meshes. Their method

optimizes deformation matrices through gradient back-propagation from rendering errors and regularization terms constraining deformation energy. Their Lagrangian representation avoids the iso-surface extraction required by Eulerian methods like DMTet and FlexiCube and circumvents grid resolution limitations. However, tetrahedral sphere representations are significantly more complex than 3D Gaussian representations, limiting applicability in large-scale scenes.

Tobiasz *et al.* [30] developed a method to convert trained GS models to mesh models through post-processing. They approximate Gaussian plates with multiple triangles and optimize triangle attributes using a differentiable renderer [20]. While their motivation resembles ours, their extracted meshes contain several times more faces than the original Gaussian count, and the triangle facelets remain transparent. In contrast, our method maintains primitive count parity with Gaussian-based methods while producing solid meshes.

## 3. Method

2D Triangle Splatting (2DTS) replace the Gaussian primitives from 3DGS [17] with triangle primitives and combines the compactness parameter from GES [12] to approximate a solid mesh representation. The triangle primitives are rendered using the splatting and alpha-blending methods introduced in 3DGS. To enable the gradient back-propagation through the rendering process, we use a decaying opacity function based on the barycentric coordinates of each point on the triangle plane. The depth and normal of each primitive can be calculated naturally from the normal of the triangle plane and the depth of the triangle vertices. A normal consistency loss similar to the one used in 2DGS [15] is applied to constrain the rendered normals and depth image. Figure 2 shows an overview of the proposed method.

### 3.1. Triangle Splatting

To render a triangle facelet, we first project the triangle to the screen space. To simplify the expressions, we ignore the triangle index in this subsection.

**Projection.** For triangles with a depth near zero in the camera space, a perspective projection will create a large distortion in the screen space. So, instead of directly projecting the triangle vertices, we project the vector from the triangle center to each vertex with a linear approximation of the perspective projection around the center, similar to the local affine mapping in EWA [37]. We denote the vector from the barycenter  $C$  of the triangle to the  $i$ -th vertex as  $\mathbf{R}^i$ , the projected barycenter on the screen space as  $\mathbf{C}_{2D}$  and the projected vector as  $\mathbf{R}_{2D}^i$ . Then we have:

$$\begin{aligned}\mathbf{C}_{2D} &= \mathbf{P}(\mathbf{C}), \\ \mathbf{R}_{2D}^i &= \mathbf{J} \cdot \mathbf{R}^i,\end{aligned}\tag{1}$$

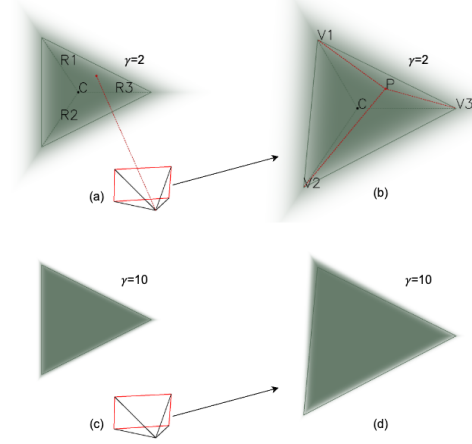


Figure 2. **Overview of the proposed 2D Triangle Splatting (2DTS) method.** First, we project each triangle to the image plane and calculate the barycentric coordinates of each pixel. Then, the opacity of each pixel is determined by an eccentricity value calculated from the barycentric coordinates. The final color of each pixel is calculated by blending the colors of all triangles that cover the pixel. A compactness parameter  $\gamma$  is introduced to control the sharpness of the triangle edges. Panel (a) and (c) shows the triangle facetlet in the 3D space, and panel (b) and (d) shows the triangle splatted on the screen space. Panel (a) and (b) shows a triangle with  $\gamma = 2$ , and panel (c) and (d) shows a triangle with  $\gamma = 10$ .

where  $\mathbf{J}$  is the Jacobian matrix of the perspective projection  $\mathbf{P}(\mathbf{u})$  given by the partial derivatives of the projection function at point  $\mathbf{C}$ :

$$\mathbf{J} = \left[ \frac{\partial \mathbf{P}(\mathbf{u})}{\partial \mathbf{u}} \right]_{\mathbf{u}=\mathbf{C}}. \quad (2)$$

To avoid the distortion mentioned above, we clip the coordinate of the point  $\mathbf{C}$  in the view space  $\mathbf{C}_v = (C_{vx}, C_{vy}, C_{vz})$  used in the derivative calculation to  $\mathbf{C}'_v = (C'_{vx}, C'_{vy}, C'_{vz})$  with:

$$\begin{aligned} \frac{C'_{vx}}{C'_{vz}} &= \min(\max(\frac{C_{vx}}{C_{vz}}, -1.3F_x), 1.3F_x), \\ \frac{C'_{vy}}{C'_{vz}} &= \min(\max(\frac{C_{vy}}{C_{vz}}, -1.3F_y), 1.3F_y), \end{aligned} \quad (3)$$

where  $F_x = \tan(\frac{F_o V_x}{2})$  and  $F_y = \tan(\frac{F_o V_y}{2})$ , respectively.

**Dilation.** In the physical process of sensor imaging, each pixel's output integrates light intensity over its entire area. All visible objects contribute to this output, even when projected to less than a pixel's size on the sensor. However, in our rendering process, pixel values are calculated only at the pixel center. Consequently, triangles smaller than a pixel that don't cover the center remain unaccounted for and receive no optimization signals during training. To better approximate the physical imaging process, we apply a dilation operation to projected triangles in screen space. Specifically, we stretch each projected vector  $\mathbf{R}_{2D}^i$  by half a pixel

length:

$$\mathbf{R}_{2D}^{i'} = \mathbf{R}_{2D}^i \cdot (1 + \frac{0.5}{|\mathbf{R}_{2D}^i|}). \quad (4)$$

The projected vertices on the screen space are calculated by:

$$\mathbf{V}_{2D}^i = \mathbf{C}_{2D} + \mathbf{R}_{2D}^{i'}.$$

**Barycentric Coordinates.** To render the triangle on the image, we calculate the barycentric coordinates  $(a_j^1, a_j^2, a_j^3)$  of each pixel  $\mathbf{P}_j$  given the screen space vertices  $\mathbf{V}_{2D}^1, \mathbf{V}_{2D}^2, \mathbf{V}_{2D}^3$ :

$$\begin{aligned} a_j^1 \cdot \mathbf{V}_{2D}^1 + a_j^2 \cdot \mathbf{V}_{2D}^2 + a_j^3 \cdot \mathbf{V}_{2D}^3 &= \mathbf{P}_j, \\ a_j^1 + a_j^2 + a_j^3 &= 1. \end{aligned} \quad (5)$$

The equations can be solved by:

$$\begin{aligned} \begin{bmatrix} a_j^1 \\ a_j^2 \end{bmatrix} &= [\mathbf{V}_{2D}^1 - \mathbf{V}_{2D}^3 \quad \mathbf{V}_{2D}^2 - \mathbf{V}_{2D}^3]^{-1} \cdot (\mathbf{P}_j - \mathbf{V}_{2D}^3), \\ a_j^3 &= 1 - a_j^1 - a_j^2. \end{aligned} \quad (6)$$

**Opacity Calculation.** To mimic the exponentially decaying opacity of the Gaussian primitives in 3DGS, we define the opacity of the triangle on each pixel  $\mathbf{o}_j$  as:

$$\begin{aligned} o_j &= O \cdot \exp(-\frac{1}{2}e_j^2\gamma), \\ e_j &= 1 - 3 \cdot \min(a_j^1, a_j^2, a_j^3). \end{aligned} \quad (7)$$

where  $O$  is the opacity property of the triangle,  $\gamma$  is the compactness parameter we use to control the sharpness of the triangle edges, and  $e_j$  is an eccentricity value similar to the quadratic function on the power term of a Gaussian kernel defined as:

$$G(\mathbf{x}) = \frac{1}{2\pi|\Sigma|^{\frac{1}{2}}} \exp(-\frac{1}{2}(\mathbf{x} - \mathbf{C})^T \Sigma (\mathbf{x} - \mathbf{C})). \quad (8)$$

**Compactness Tuning.** The eccentricity value  $e_j$  defined above separates the screen space into three regions divided by  $\mathbf{R}_{2D}^1, \mathbf{R}_{2D}^2$  and  $\mathbf{R}_{2D}^3$ , and increase monotonically as the distance from  $\mathbf{P}_j$  to the edge of the triangle on that region decrease (for example, the distance between  $\mathbf{P}$  and  $\mathbf{V}_1\mathbf{V}_3$  in Figure 2(b)).  $e_j$  satisfies that  $0 \leq e_j < 1$  for points inside the triangle,  $e_j = 1$  for points on the edge of the triangle, and  $e_j > 1$  for points outside the triangle. So, we have:

$$o_j|_{\gamma \rightarrow \infty, O \rightarrow 1} = \begin{cases} 1, & \mathbf{P}_j \text{ inside,} \\ 0, & \mathbf{P}_j \text{ outside.} \end{cases} \quad (9)$$

By gradually increasing the compactness parameter  $\gamma$  and constraining  $O$  to 1, we can approximate a solid triangle mesh representation at the end of the training, as shown in Figure 2(c)(d).

**Scale Compensation.** During the increase of  $\gamma$ , the effective area covered by each triangle naturally shrinks. To



maintain consistent coverage throughout the compactness tuning process, we implement a scale compensation mechanism based on an invariant opacity integration principle.

Mathematically, we aim to preserve the integration of opacity over the triangle plane regardless of the compactness parameter  $\gamma$ . The integration can be calculated analytically as:

$$I(S, \gamma) = \int_{\Delta} o_j dA = S \cdot O \cdot \frac{2^{\frac{1}{\gamma}} \Gamma(\frac{1}{\gamma})}{\gamma}, \quad (10)$$

where  $S$  is the triangle area,  $\Gamma(x)$  is the Euler's Gamma function, and  $o_j$  and  $O$  are defined in Equation 7. The detailed derivation of this integration is provided in the supplementary materials.

As  $\gamma$  approaches infinity, the integration becomes  $I(S_0, \infty) = S_0 \cdot O$ , with  $S_0$  representing the solid triangle area. To ensure invariance across different  $\gamma$  values, we apply a scale factor:

$$S(\gamma) = S_0 \cdot \frac{\gamma}{2^{\frac{1}{\gamma}} \Gamma(\frac{1}{\gamma})}. \quad (11)$$

This compensation ensures that triangles maintain their effective coverage throughout the optimization process, enabling smooth transition toward the solid mesh representation.

### 3.2. Alpha-Blending

To render the final image, the triangles are first sorted by the depth of the barycenter in the camera space and then alpha-blended from front to back, similar to the alpha-blending process in 3DGS. The final color  $c_j$  of each pixel  $P_j$  is calculated by blending the colors of all triangles that cover the pixel:

$$c_j = \sum_{i=1}^N c^i \cdot o_j^i \prod_{k=1}^{i-1} (1 - o_j^k), \quad (12)$$

where  $c^i$  is the color of the  $i$ -th triangle, and  $o_j^i$  is the opacity of the  $i$ -th triangle on the pixel  $P_j$ , as defined in Equation 7. The color  $c^i$  can either be a native attribute of the triangle or evaluated from a set of spherical harmonic coefficients and the viewing direction, as introduced by Yu *et al.* [6].

**Depth and Normal Rendering.** The depth  $d_j$  and normal  $n_j$  of each pixel is also rendered through the alpha-blending process:

$$d_j = \sum_{i=1}^N d_j^i \cdot o_j^i \prod_{k=1}^{i-1} (1 - o_j^k), \quad (13)$$

$$n_j = \text{norm} \left( \sum_{i=1}^N n^i \cdot o_j^i \prod_{k=1}^{i-1} (1 - o_j^k) \right).$$

where  $n^i$  is the normal of the  $i$ -th triangle in the camera space defined as:

$$n^i = (\mathbf{V}_{view}^2 - \mathbf{V}_{view}^1) \times (\mathbf{V}_{view}^3 - \mathbf{V}_{view}^1). \quad (14)$$

We don't normalize the normal vector before alpha-blending so that the normal blending is weighted by the area of the triangles. The weighting effectively applies a low-pass filter to the normal rendering, reducing the noise from small triangles.  $d_j^i$  is defined naturally as the depth of the intersection point of the ray from the camera center to the pixel  $P_j$  and the  $i$ -th triangle plane, as shown in Figure 2(a). It can be approximated in our splatting configuration by:

$$d_j^i = a_j^{i1} \cdot d^{i1} + a_j^{i2} \cdot d^{i2} + a_j^{i3} \cdot d^{i3}, \quad (15)$$

where  $d^{i1}, d^{i2}, d^{i3}$  are the depth of the  $i$ -th triangle vertices in the camera space, and  $a_j^{i1}, a_j^{i2}, a_j^{i3}$  are the barycentric coordinates of  $P_j$  on  $i$ -th triangle from Equation 5.

### 3.3. Optimization

Because the rendered color, normal and depth images are differentiable with respect to the triangle vertices, opacities and colors, we can optimize the triangle attributes by minimizing a loss function defined on the rendered images.

**Normal Consistency.** We use a normal consistency loss similar to the one used in 2DGS [15] to constrain the rendered normal and depth image. Given a rendered depth image  $d_j$ , we can infer a camera space normal image  $n'_j$  by calculating the depth gradient. We leave the details of the derivation to the supplementary materials. With the rendered normal  $n_j$  and the inferred normal  $n'_j$ , we define the normal consistency loss as:

$$\mathcal{L}_n = \frac{1}{N} \sum_{j=1}^N (1 - n_j \cdot n'_j). \quad (16)$$

**Opacity Regularization.** There is an inherent conflict between differentiable training and the solid mesh representation. When taking the limit of  $\gamma \rightarrow \infty$  and  $O \rightarrow 1$  in Equation 9, the gradients for triangle vertices diminish to zero. To address this challenge, we employ a progressive strategy to gradually increase the compactness parameter  $\gamma$ . Additionally, we provide two different approaches to ensure triangle opacities converge to 1 by the end of training: opacity tuning and straight through estimator (STE). We divide the training process into three distinct stages.

In the first stage, we set  $\gamma = 1$  and apply a quadratic opacity regularization loss:

$$\mathcal{L}_o = \frac{1}{N} \sum_{i=1}^N (0.25 - (o_i - 0.5)^2) \quad (17)$$

This encourages opacities to polarize toward either 0 or 1.

In the second stage, we solidify the triangles by gradually increasing  $\gamma$  from 1 to  $\gamma_{\text{end}}$  following an exponential schedule. For the opacity tuning approach, we implement a pruning and clipping strategy that removes triangles with opacity below threshold  $T_{\text{low}}$  and clips opacities above

threshold  $T_{\text{high}}$  to 1. We progressively increase  $T_{\text{low}}$  from 0 to 0.5 and decrease  $T_{\text{high}}$  from 1 to 0.5 using an exponential schedule. For the STE approach, we utilize the straight through estimator defined as:

$$\text{STE}(O_i) = (\text{Sign}(O_i - O_{\text{thres}}) - O_i) \cdot \text{detach}() + O_i, \quad (18)$$

This allows triangles to have binary opacities while maintaining gradient flow during backpropagation. Triangles with opacity below  $O_{\text{thres}}$  are pruned upon completion of training. Both methods ensure triangle opacities converge to 1 after training.

In the third stage, we fix  $\gamma = \gamma_{\text{end}}$  and  $O = 1$  and fine-tune the model with extra training steps. In our experiments, we observe a recovery of the PSNR score with this fine-tuning step from the loss during the solidification process in the second stage.

**Loss Function.** We use an L1 loss and an SSIM loss to optimize the rendered color image  $c_j$  to the ground truth color image  $c_j^{\text{gt}}$ :

$$\mathcal{L}_{L1} = \frac{1}{N} \sum_{j=1}^N (\|c_j - c_j^{\text{gt}}\|_1), \quad (19)$$

$$\mathcal{L}_{SSIM} = 1 - \text{SSIM}(c_j, c_j^{\text{gt}}),$$

The final loss function is defined as:

$$\mathcal{L} = \lambda_{L1} \mathcal{L}_{L1} + \lambda_{SSIM} \mathcal{L}_{SSIM} + \lambda_n \mathcal{L}_n + \lambda_o \mathcal{L}_o, \quad (20)$$

where  $\lambda_{L1}$ ,  $\lambda_{SSIM}$ ,  $\lambda_n$  and  $\lambda_o$  are the weights of the corresponding loss terms.

### 3.4. Mesh Saving

Our proposed 2DTS method naturally forms a mesh-like structure. We save each triangle facelet in our model as a mesh face and set the face color as the RGB color of the triangle. Higher SH coefficients, the opacity and the compactness parameter are discarded in the mesh representation. The mesh is exported in the GLB format, which can be directly loaded into most 3D rendering engines.

## 4. Experiments

We conduct experiments of two categories. We first compare the vanilla version of our method, in which we fix the compactness parameter  $\gamma$  to 1 and applies no opacity regularization, with state-of-the-art Gaussian-based methods on the MipNeRF-360 dataset [2]. We then compare the mesh extracted from our method with the mesh extracted from 2DGS [15] and Nvdiffrac [25], which are strong baselines for Gaussian-based methods and mesh-based methods, respectively. The mesh extraction comparison is tested on both object-centric datasets and large-scale city datasets to demonstrate the generalization of our method.

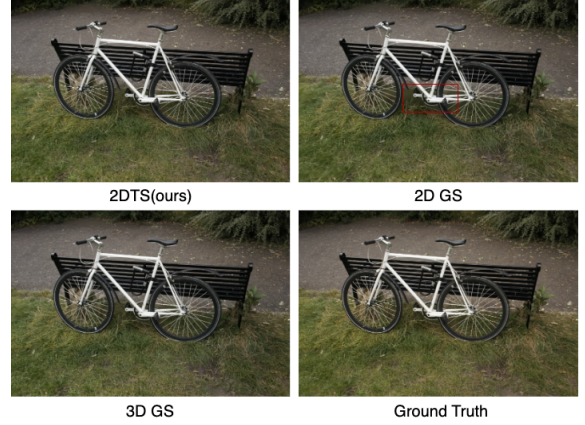


Figure 3. **Comparison of the radiance field reconstruction between 2DTS, 3DGS and 2DGS.** Visual comparison of our 2DTS method against 3DGS [17] and 2DGS [15] on the Mip-NeRF360 [2] dataset. Only one view is shown for each method due to space constraints. Please refer to the supplementary materials for more views.

### 4.1. Implementation

We implement the 2D triangle splatting rasterizer with custom CUDA kernels, based on the code provided by 3DGS [17]. For all experiments, we initialize our triangle primitives from the point cloud by setting the barycenter and spherical harmonic coefficients of each triangle according to the location and color of the corresponding point. Each triangle is initialized as an equilateral triangle with a scale proportional to the distance between the point and its nearest neighbor. The normal of each triangle is initialized randomly. We did not implement any densification strategy during training, instead, we densify the point cloud before training and only prune the triangles during training.

We use the Adam optimizer to optimize the parameters of the triangle primitives. The learning rates are modulated by exponential decay schedules. Please refer to our code for the detailed learning rate settings. All our experiments run on a single NVIDIA H20 GPU with 96 GB memory.

### 4.2. Triangle and Gaussian Splatting

We first compare our method’s vanilla version against 3DGS [17] and 2DGS [15] on Mip-NeRF360 [2], NeRF-Synthetic [24], Tanks and Temples [18], and Deep Blending [13] datasets. For Mip-NeRF360, we downsample indoor scene images by a factor of two and outdoor scene images by a factor of four. Images from other datasets are used as provided. We create train/test splits by selecting every 8th photo as a test image for Mip-NeRF360, Tanks and Temples, and Deep Blending datasets, while using the provided split for NeRF-Synthetic. All experiments run for 30k iterations with a batch size of 1. In the vanilla version, we disable compactness tuning, normal consistency loss, and opacity regularization. The maximum degree of spherical

	Mip-NeRF360 Outdoor Scene			Mip-NeRF360 Indoor Scene			NeRF-Synthetic			Tanks & Temples			Deep Blending		
	PSNR $\uparrow$	SSIM $\uparrow$	LIPPS $\downarrow$	PSNR $\uparrow$	SSIM $\uparrow$	LIPPS $\downarrow$	PSNR $\uparrow$	SSIM $\uparrow$	LIPPS $\downarrow$	PSNR $\uparrow$	SSIM $\uparrow$	LIPPS $\downarrow$	PSNR $\uparrow$	SSIM $\uparrow$	LIPPS $\downarrow$
3DGS	24.71	0.732	0.226	31.35	0.927	0.181	33.26	0.969	0.030	23.96	0.855	0.160	29.86	0.904	0.242
2DGS	24.65	0.727	0.225	30.53	0.919	0.193	33.24	0.968	0.031	23.59	0.846	0.180	29.95	0.905	0.242
2DTS (Ours)	25.58	0.758	0.226	31.06	0.935	0.151	33.46	0.969	0.031	23.87	0.869	0.209	29.89	0.905	0.128

Table 1. Quantitative comparison of the radiance field reconstruction of 3DGS, 2DGS and 2DTS on Mip-NeRF360 [2], NeRF-Synthetic [24], Deep Blending [13] and Tanks & Temples [18] datasets. Red indicates the best score.

harmonic coefficients is set to 3, matching the configurations of the compared methods. The densification process is turned off, and the same dense initial point cloud is used for all methods. The initial point cloud is converted from a trained GS model.

Table 1 presents the quantitative results, with qualitative comparisons shown in Figure 3. Our method outperforms 3DGS and 2DGS in most metrics. However, we want to highlight that our main focus is on the geometric and visual accuracy of the reconstructed meshes presented in the next section. We provide the radiance field comparison here for completeness.

#### 4.3. Mesh Extraction on Small Scenes

We compare the visual quality of meshes extracted from our method with those from 2DGS [15] and Nvdiffrac [25] on the NeRF-Synthetic dataset [24], which contains 360-degree views of small objects. The meshes from our method and the 2DGS method are simple mesh with vertices location and face color, while the meshes from Nvdiffrac contains full PBR material and lighting information. The mesh from 2DGS is extracted using the TSDF method with the authors’ official code. We use the custom renderer provided by Nvdiffrac, which accounts for the PBR material and lighting information, to render the meshes into images and calculate PSNR, SSIM, and LIPPS metrics against ground truth images. For the 2DGS method, we use the Kaolin library [7] to render the mesh since it does not provide a custom renderer. The rendering result for our method is rendered by our custom 2DTS renderer.

Our experiments run for 60K iterations with a batch size of 1. The training process follows the three stages described in Section 3.3, with 20K iterations for each stage. We apply the STE method (detailed in Section 3.3) to regularize triangle opacity throughout these experiments. During the second and third stages, we set the ending compactness parameter  $\gamma_{\text{end}}$  to 50. Normal consistency loss is disabled for these small scene experiments. For mesh extraction, we set the maximum degree of spherical harmonic coefficients to 0, as standard mesh formats only support RGB color values.

The quantitative results are shown in Table 2, with qualitative comparisons in Figure 4. The quantitative results contain visual metrics (PSNR, SSIM, and LIPPS), geometric metrics (Chamfer Distance (CD) and triangle count), and resource usage (GPU memory and time). Our method pro-

duces meshes with comparable visual quality (PSNR) and superior geometric accuracy (CD) compared to Nvdiffrac. Our method outperforms 2DGS on both visual and geometric metrics, while producing much sparser meshes.

Notably, in the visual comparison, our method better preserves thin structures such as the leaves, wires and ropes compared to other methods. Please also see Figure 1 for a zoomed-in wireframe comparison of the reconstructed mesh on the ship scene.

#### 4.4. Mesh Extraction on Large Scenes

We extend our experiments from Section 4.3 to the MatrixCity dataset [21], which contains large-scale city scenes, to demonstrate the scalability of our approach.

Due to the significantly higher view count in the MatrixCity dataset compared to NeRF-Synthetic, we increase the training iterations to 90K, with each of the three stages running for 30K iterations. The ending compactness parameter  $\gamma_{\text{end}}$  is kept at 50, while opacity tuning method is applied for regularization (see Section 3.3). We also incorporate normal consistency loss in these large scene experiments to leverage the flat surface inductive bias prevalent in urban environments.

In our experiments, Nvdiffrac fails to generalize to MatrixCity due to its grid-based limitations, resulting in single-digit PSNR scores and non-converging training losses even with doubled dmtet-grid resolution. For the 2DGS method, we adjusted the grid resolution of the TSDF mesh extraction process to prevent memory overflow. The quantitative results are presented in Table 2, and we leave qualitative comparisons to the supplementary materials because of the space limitation.

#### 4.5. Relighting and Ablation Study

To demonstrate the practical applications of our method in rendering scenarios, we present results of meshes extracted from the MatrixCity dataset rendered under various lighting conditions. Additionally, we conduct an ablation study to evaluate the impact of our normal consistency loss on rendering quality. The meshes are rendered using the Blender Cycles renderer, with results shown in Figure 5. The face colors are treated as diffuse albedo during rendering.

Our experiments clearly demonstrate that meshes trained with normal consistency loss contains significantly less noise and smoother surfaces compared to those trained

	NeRF-Synthetic							MatrixCity						
	PSNR $\uparrow$	SSIM $\uparrow$	LIPPS $\downarrow$	CD(1e-3) $\downarrow$	Count(K) $\downarrow$	Mem(GB) $\downarrow$	Time(min) $\downarrow$	PSNR $\uparrow$	SSIM $\uparrow$	LIPPS $\downarrow$	CD(1e-3) $\downarrow$	Count(K) $\downarrow$	Mem(GB) $\downarrow$	Time(min) $\downarrow$
Nvdiffrec-Mesh	<b>29.05</b>	0.939	0.081	72.5	81	19.40	85	N.A.	N.A.	N.A.	N.A.	N.A.	N.A.	N.A.
2DGS-Mesh	22.11	0.871	0.130	116.7	574	<b>2.13</b>	81	20.86	0.578	0.553	5.26	14239	<b>31.76</b>	288
2DTS-Mesh (Ours)	28.79	<b>0.945</b>	<b>0.077</b>	<b>51.9</b>	<b>68</b>	2.85	<b>28</b>	<b>24.15</b>	<b>0.716</b>	<b>0.457</b>	<b>0.83</b>	<b>5772</b>	33.24	<b>131</b>

Table 2. Mesh reconstruction result of Nvdiffrec, 2DGS and 2DTS on the NeRF-Synthetic and MatrixCity datasets. NeRF-Synthetic shows arithmetic averages. Time includes mesh extraction if applicable. Memory only accounts for GPU usage, note that 2DGS used 5(NeRF-Synthetic)-60(MatrixCity) GB of CPU memory for mesh extraction. CD stands for Chamfer Distance. Sample count for CD is 2.5M on NeRF-Synthetic and 10M on MatrixCity. Counts are the number of triangles in the extracted mesh. Red indicates the best score.



Figure 4. **Comparison of Mesh Extraction.** Visual quality comparison of meshes extracted from our method, 2DGS [15], and Nvdiffrec [25] on the NeRF-Synthetic [24] dataset.

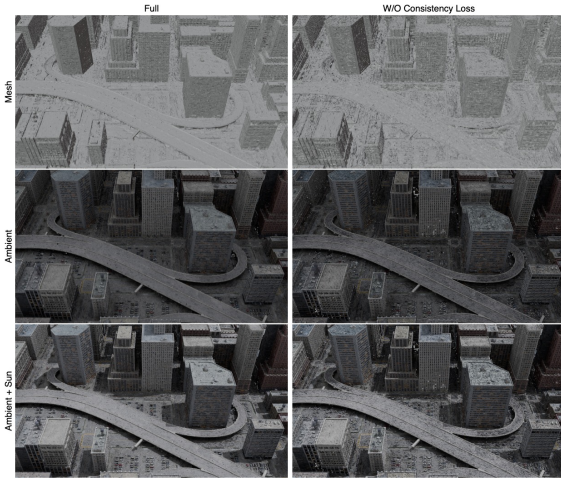


Figure 5. **Relighting Results on MatrixCity Dataset.** Comparison of meshes extracted from the MatrixCity dataset rendered under two lighting conditions: ambient-only lighting (middle) and combined ambient with directional sunlight (bottom). The top row shows the reconstructed meshes. The left column shows our full model, while the right column shows results without normal consistency loss.

without this constraint. This quality difference becomes particularly apparent under directional lighting, where the

consistent normals produce more visually coherent and realistic renderings.

## 5. Conclusion

We present a novel method for mesh reconstruction from multiview images using 2D triangle splatting. This approach successfully combines the visual fidelity of radiance-field-based representations with the portability and efficiency of mesh-based representations. Our experiments demonstrate that our method surpasses other state-of-the-art differentiable mesh reconstruction methods in terms of visual quality and geometric accuracy. We emphasize that, to our knowledge, our method is the first to achieve differentiable mesh reconstruction without relying on any form of vertex grid. This grid-free design is crucial for large-scale scene applications, enabling more flexible and efficient representation of varying detail levels. We believe our method has significant potential for a wide range of applications, including 3D map reconstruction and virtual reality. The code will be made publicly available.

**Limitations and Future Work.** Our current approach requires a well-reconstructed point cloud as initialization. We have not yet explored adaptive point cloud densification during training, as we aimed to control variables while com-



paring with state-of-the-art Gaussian-based methods. In future work, a densification strategy based on gradient magnitude, similar to that used in 3DGS [17], could be adapted to our method. Additionally, as discussed in the experiments section, the meshes produced by our method are not watertight, limiting their applicability in simulation-related tasks. Integrating a stitching process that encourages triangles to share vertices and edges could yield meshes with improved topology.

**Ethics Statement.** The proposed method could potentially be misused for generating fake 3D models of real-world objects or unauthorized large-scale mapping. However, these concerns apply equally to all existing 3D reconstruction methods and are not specific to our approach. We believe the benefits of our contribution outweigh these potential risks.

## References

- [1] Jonathan T. Barron, Ben Mildenhall, Matthew Tancik, Peter Hedman, Ricardo Martin-Brualla, and Pratul P. Srinivasan. Mip-NeRF: A multiscale representation for anti-aliasing neural radiance fields, 2021. 2
- [2] Jonathan T. Barron, Ben Mildenhall, Dor Verbin, Pratul P. Srinivasan, and Peter Hedman. Mip-NeRF 360: Unbounded anti-aliased neural radiance fields. *CVPR*, 2022. 2, 6, 7, 11, 12
- [3] Danpeng Chen, Hai Li, Weicai Ye, Yifan Wang, Weijian Xie, Shangjin Zhai, Nan Wang, Haomin Liu, Hujun Bao, and Guofeng Zhang. PGSR: Planar-based gaussian splatting for efficient and high-fidelity surface reconstruction. *IEEE Transactions on Visualization and Computer Graphics*, pages 1–12, 2024. 1, 3
- [4] Rui Chen, Songfang Han, Jing Xu, and Hao Su. Point-based multi-view stereo network. In *The IEEE International Conference on Computer Vision (ICCV)*, 2019. 2
- [5] Zhiqin Chen, Thomas Funkhouser, Peter Hedman, and Andrea Tagliasacchi. MobileNeRF: Exploiting the polygon rasterization pipeline for efficient neural field rendering on mobile architectures. In *The Conference on Computer Vision and Pattern Recognition (CVPR)*, 2023. 3
- [6] Sara Fridovich-Keil, Alex Yu, Matthew Tancik, Qinhong Chen, Benjamin Recht, and Angjoo Kanazawa. Plenoxels: Radiance fields without neural networks. In *CVPR*, 2022. 5
- [7] Clement Fuji Tsang, Maria Shugrina, Jean Francois Lafleche, Or Perel, Charles Loop, Towaki Takikawa, Vismay Modi, Alexander Zook, Jiehan Wang, Wenzheng Chen, Tianchang Shen, Jun Gao, Krishna Murthy Jatavallabhula, Edward Smith, Artem Rozantsev, Sanja Fidler, Gavriel State, Jason Gorski, Tommy Xiang, Jianing Li, Michael Li, and Rev Lebaredian. Kaolin: A pytorch library for accelerating 3d deep learning research. 7
- [8] Yasutaka Furukawa and Carlos Hernández. Multi-view stereo: A tutorial. *Foundations and Trends® in Computer Graphics and Vision*, 9(1-2):1–148, 2015. 2
- [9] Yasutaka Furukawa and Jean Ponce. Accurate, dense, and robust multiview stereopsis. *IEEE Transactions on Pattern Analysis and Machine Intelligence*, 32(8):1362–1376, 2010. 2
- [10] Jian Gao, Chun Gu, Youtian Lin, Zhihao Li, Hao Zhu, Xun Cao, Li Zhang, and Yao Yao. Relightable 3D Gaussians: Realistic point cloud relighting with BRDF decomposition and ray tracing. In *ECCV*, pages 73–89, Berlin, Heidelberg, 2024. Springer-Verlag. 1
- [11] Minghao Guo, Bohan Wang, Kaiming He, and Wojciech Matusik. TetSphere Splatting: Representing high-quality geometry with Lagrangian volumetric meshes. In *The Thirtieth International Conference on Learning Representations*, 2025. 1, 3
- [12] Abdullah Hamdi, Luke Melas-Kyriazi, Jinjie Mai, Guocheng Qian, Ruoshi Liu, Carl Vondrick, Bernard Ghanem, and Andrea Vedaldi. GES: Generalized exponential splatting for efficient radiance field rendering. In *Proceedings of the IEEE/CVF Conference on Computer Vision and Pattern Recognition (CVPR)*, pages 19812–19822, 2024. 2, 3
- [13] Peter Hedman, Julien Philip, True Price, Jan-Michael Frahm, George Drettakis, and Gabriel Brostow. Deep blending for free-viewpoint image-based rendering. *ACM Transactions on Graphics (Proc. SIGGRAPH Asia)*, 37(6):257:1–257:15, 2018. 6, 11, 13, 14. 6, 7, 11, 12
- [14] Jan Held, Renaud Vandeghen, Abdullah Hamdi, Adrien Deli'ege, Anthony Cioppa, Silvio Giancola, Andrea Vedaldi, Bernard Ghanem, and Marc Van Droogenbroeck. 3D convex splatting: Radiance field rendering with 3D smooth convexes. *arXiv*, abs/2411.14974, 2024. 1, 3
- [15] Binbin Huang, Zehao Yu, Anpei Chen, Andreas Geiger, and Shenghua Gao. 2D gaussian splatting for geometrically accurate radiance fields. In *SIGGRAPH 2024 Conference Papers*. Association for Computing Machinery, 2024. 1, 2, 3, 5, 6, 7, 8, 12, 13
- [16] Abhishek Kar, Christian Häne, and Jitendra Malik. Learning a multi-view stereo machine. In *Advances in Neural Information Processing Systems*. Curran Associates, Inc., 2017. 2
- [17] Bernhard Kerbl, Georgios Kopanas, Thomas Leimkühler, and George Drettakis. 3D gaussian splatting for real-time radiance field rendering. *ACM Transactions on Graphics*, 42(4), 2023. 1, 2, 3, 6, 9, 12
- [18] Arno Knapitsch, Jaesik Park, Qian-Yi Zhou, and Vladlen Koltun. Tanks and temples: Benchmarking large-scale scene reconstruction. *ACM Transactions on Graphics (ToG)*, 36(4):1–13, 2017. 6, 11, 13, 14. 6, 7, 11, 12
- [19] K.N. Kutulakos and S.M. Seitz. A theory of shape by space carving. In *Proceedings of the Seventh IEEE International Conference on Computer Vision*, pages 307–314 vol.1, 1999. 2
- [20] Samuli Laine, Janne Hellsten, Tero Karras, Yeongho Seol, Jaakko Lehtinen, and Timo Aila. Modular primitives for high-performance differentiable rendering. *ACM Transactions on Graphics*, 39(6), 2020. 3
- [21] Yixuan Li, Lihan Jiang, Linning Xu, Yuanbo Xiangli, Zhenzhi Wang, Dahua Lin, and Bo Dai. Matrixcity: A large-scale city dataset for city-scale neural rendering and beyond. In *Proceedings of the IEEE/CVF International Conference on Computer Vision*, pages 3205–3215, 2023. 7, 12, 13

- [22] Weikai Lin, Yu Feng, and Yuhao Zhu. MetaSapiens: Real-time neural rendering with efficiency-aware pruning and accelerated foveated rendering, 2024. [1](#)
- [23] William E. Lorensen and Harvey E. Cline. Marching cubes: A high resolution 3d surface construction algorithm. *SIG-GRAPH Comput. Graph.*, 21(4):163–169, 1987. [2](#)
- [24] Ben Mildenhall, Pratul P. Srinivasan, Matthew Tancik, Jonathan T. Barron, Ravi Ramamoorthi, and Ren Ng. NeRF: Representing scenes as neural radiance fields for view synthesis. In *ECCV*, 2020. [1](#), [2](#), [6](#), [7](#), [8](#), [11](#), [12](#)
- [25] Jacob Munkberg, Jon Hasselgren, Tianchang Shen, Jun Gao, Wenzheng Chen, Alex Evans, Thomas Müller, and Sanja Fidler. Extracting Triangular 3D Models, Materials, and Lighting From Images. In *Proceedings of the IEEE/CVF Conference on Computer Vision and Pattern Recognition (CVPR)*, pages 8280–8290, 2022. [2](#), [3](#), [6](#), [7](#), [8](#)
- [26] Richard A. Newcombe, Shahram Izadi, Otmar Hilliges, David Molyneaux, David Kim, Andrew J. Davison, Pushmeet Kohi, Jamie Shotton, Steve Hodges, and Andrew Fitzgibbon. KinectFusion: Real-time dense surface mapping and tracking. In *2011 10th IEEE International Symposium on Mixed and Augmented Reality*, pages 127–136, 2011. [1](#), [3](#)
- [27] Johannes L. Schönberger, Enliang Zheng, Jan-Michael Frahm, and Marc Pollefeys. Pixelwise view selection for unstructured multi-view stereo. In *Computer Vision – ECCV 2016*, pages 501–518, Cham, 2016. Springer International Publishing. [1](#), [2](#)
- [28] Tianchang Shen, Jun Gao, Kangxue Yin, Ming-Yu Liu, and Sanja Fidler. Deep marching tetrahedra: a hybrid representation for high-resolution 3d shape synthesis. In *Advances in Neural Information Processing Systems (NeurIPS)*, 2021. [3](#)
- [29] Tianchang Shen, Jacob Munkberg, Jon Hasselgren, Kangxue Yin, Zian Wang, Wenzheng Chen, Zan Gojcic, Sanja Fidler, Nicholas Sharp, and Jun Gao. Flexible isosurface extraction for gradient-based mesh optimization. *ACM Trans. Graph.*, 42(4), 2023. [3](#)
- [30] Rafał Tobiasz, Grzegorz Wilczyński, Marcin Mazur, Sławomir Tadeja, and Przemysław Spurek. MeshSplats: Mesh-based rendering with gaussian splatting initialization, 2025. [3](#)
- [31] Yao Yao, Zixin Luo, Shiwei Li, Tian Fang, and Long Quan. Mvsnet: Depth inference for unstructured multi-view stereo. *European Conference on Computer Vision (ECCV)*, 2018. [2](#)
- [32] Mulin Yu, Tao Lu, Linning Xu, Lihan Jiang, Yuanbo Xiangli, and Bo Dai. GSDF: 3DGS meets SDF for improved neural rendering and reconstruction. In *Advances in Neural Information Processing Systems*, pages 129507–129530. Curran Associates, Inc., 2024. [3](#)
- [33] Zehao Yu, Anpei Chen, Binbin Huang, Torsten Sattler, and Andreas Geiger. Mip-Splatting: Alias-free 3D gaussian splatting. *Conference on Computer Vision and Pattern Recognition (CVPR)*, 2024. [2](#)
- [34] Baowen Zhang, Chuan Fang, Rakesh Shrestha, Yixun Liang, Xiaoxiao Long, and Ping Tan. RaDe-GS: Rasterizing depth in gaussian splatting, 2024. [1](#), [3](#)
- [35] Wenyuan Zhang, Yu-Shen Liu, and Zhizhong Han. Neural signed distance function inference through splatting 3d gaussians pulled on zero-level set. In *Advances in Neural Information Processing Systems*, 2024. [3](#)
- [36] Qian-Yi Zhou, Jaesik Park, and Vladlen Koltun. Open3D: A modern library for 3D data processing. *arXiv:1801.09847*, 2018. [1](#), [3](#)
- [37] M. Zwicker, H. Pfister, J. van Baar, and M. Gross. Ewa volume splatting. In *Proceedings Visualization, 2001. VIS '01.*, pages 29–538, 2001. [3](#)

## A. Detailed Proof of Equations

### A.1. Render Normal from Depth

Given a rendered depth image  $d_j$ , we can infer a camera space normal image  $\mathbf{n}'_j$  as follows. We first define:

$$\begin{aligned} \mathbf{D}_j &= [D_x, D_y] |_{\mathbf{P}_j} = \left[ \frac{1}{d} \frac{\partial d}{\partial x}, \frac{1}{d} \frac{\partial d}{\partial y} \right] |_{\mathbf{P}_j}, \\ \mathbf{n}'_j &= \text{norm} \left( [n'_x, n'_y, n'_z] |_{\mathbf{P}_j} \right), \end{aligned} \quad (21)$$

where  $\frac{\partial d}{\partial x}$  and  $\frac{\partial d}{\partial y}$  are the depth gradient on the pixel  $\mathbf{P}_j$  defined as the difference between the depth of adjacent pixels, which we calculate with a Scharr Filter. Then, we have:

$$\begin{aligned} n'_x &= \frac{WD_x}{2F_x}, \\ n'_y &= \frac{HD_y}{2F_y}, \\ n'_z &= 1 + D_x \left( x - \frac{W}{2} + 0.5 \right) + D_y \left( y - \frac{H}{2} + 0.5 \right), \end{aligned} \quad (22)$$

where  $W$  and  $H$  are the width and height of the image,  $x$  and  $y$  are the pixel coordinates,  $F_x = \tan(\frac{FoV_x}{2})$  and  $F_y = \tan(\frac{FoV_y}{2})$ .

### A.2. Integration of Opacity

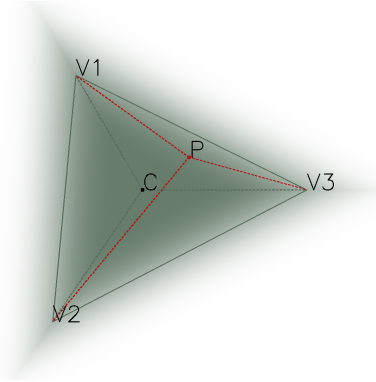


Figure 6. Auxiliary Chart for the Integration of Opacity.

We provide the detailed derivation of the integration of opacity over the triangle plane used in the *Scale Compensation* section of the main paper.

$$I(\gamma) = \int_{\Delta} o_j dA = \int_{\Delta} O \cdot \exp(-\frac{1}{2}e_j^{2\gamma}) dA \quad (23)$$

We calculate the integration separately for the three subregions of the triangle divided by  $\overline{CV_1}$ ,  $\overline{CV_2}$ , and  $\overline{CV_3}$ , as shown in Figure 6. For the subregion enclosed by  $\overline{CV_1}$  and  $\overline{CV_2}$ , we can transform the integration over area to integration over distance  $h$  to the edge  $\overline{V_1V_2}$  since the opacity is constant at each point on a line parallel to  $\overline{V_1V_2}$  in this subregion. So we have:

$$\begin{aligned} I_{\overline{CV_1}\overline{CV_2}}(\gamma) &= \int_{-\infty}^H O \cdot \exp(-\frac{1}{2}e^{2\gamma}(h)) \frac{H-h}{H} L_{\overline{V_1V_2}} dh \\ &= \int_{-\infty}^H O \cdot \exp(-\frac{1}{2}(1-\frac{h}{H})^{2\gamma})(1-\frac{h}{H}) L_{\overline{V_1V_2}} dh \\ &= \int_0^{\infty} \frac{1}{2} O \cdot H \cdot L_{\overline{V_1V_2}} \exp(-\frac{1}{2}x^{2\gamma}) dx \\ &= \frac{2^{\frac{1}{\gamma}} O \cdot S}{3} \int_0^{\infty} \exp(-x^{2\gamma}) dx \\ &= \frac{2^{\frac{1}{\gamma}} O \cdot S}{3} \frac{1}{\gamma} \Gamma(\frac{1}{\gamma}) \end{aligned} \quad (24)$$

where  $H$  is distance from  $C$  to  $\overline{V_1V_2}$ ,  $L_{\overline{V_1V_2}}$  is the length of  $\overline{V_1V_2}$ , and  $S = \frac{3}{2} L_{\overline{V_1V_2}} H$  is the area of  $\triangle V_1V_2V_3$ . The Euler's gamma function  $\Gamma$  is defined as:

$$\Gamma(x) = \int_0^{\infty} t^{x-1} e^{-t} dt.$$

Since the above integration is the same for all three subregions of the triangle plane, we have:

$$I(\gamma) = 3I_{\overline{CV_1}\overline{CV_2}}(\gamma) = O \cdot S \cdot \frac{2^{\frac{1}{\gamma}} \Gamma(\frac{1}{\gamma})}{\gamma}. \quad (25)$$

## B. Additional Experimental Results

### B.1. Triangle and Gaussian Splatting

We provide the detailed results of our experiments on each scene of the MipNeRF360 [2], NeRF-Synthetic [24], Tanks and Temples [18], and Deep Blending [13] datasets. The experiments are described in the *Triangle and Gaussian Splatting* section of the main paper.

Table 3 shows the results for the MipNeRF360 dataset, Table 4 shows the results for the NeRF-Synthetic dataset, and Table 5 shows the results for the Tanks and Temples and Deep Blending datasets. **Red** indicates the best score in these tables. The qualitative results are shown in Figure 7.

		Outdoor Scene					Indoor scene				mean
		bicycle	flowers	garden	stump	trehill	room	counter	kitchen	bonsai	
PSNR	3DGS	25.14	21.65	27.67	26.66	22.44	31.93	29.26	31.59	32.61	27.66
	2DGS	25.07	21.56	27.22	26.67	22.74	31.31	28.43	30.75	31.62	27.26
	2DTS(Ours)	<b>26.36</b>	<b>22.52</b>	<b>28.40</b>	<b>27.18</b>	<b>23.46</b>	31.74	29.04	31.38	32.07	<b>28.02</b>
SSIM	3DGS	0.767	0.613	0.873	0.776	0.628	0.922	0.911	0.929	0.944	0.818
	2DGS	0.761	0.603	0.862	0.777	0.629	0.914	0.903	0.924	0.937	0.812
	2DTS(Ours)	<b>0.795</b>	<b>0.642</b>	<b>0.884</b>	<b>0.789</b>	<b>0.681</b>	<b>0.936</b>	<b>0.918</b>	<b>0.938</b>	<b>0.948</b>	<b>0.837</b>
LPIPS	3DGS	0.193	0.321	0.098	0.304	0.315	0.210	0.194	0.122	0.197	0.206
	2DGS	0.211	0.337	0.111	0.217	0.330	0.225	0.206	0.130	0.212	0.220
	2DTS(Ours)	<b>0.191</b>	<b>0.319</b>	<b>0.096</b>	0.213	<b>0.312</b>	<b>0.170</b>	<b>0.169</b>	<b>0.106</b>	<b>0.160</b>	<b>0.193</b>

Table 3. PSNR  $\uparrow$ , SSIM  $\uparrow$ , LIPPS  $\downarrow$  scores for MipNeRF360[2] dataset.

### B.2. Mesh Extraction on Small Scenes

We provide the detailed results of our experiments on each scene of the Nerf-synthetic [24] dataset. The experiments are described in the *Mesh Extraction on Small Scenes* section of the main paper. The results are shown in Table 6.



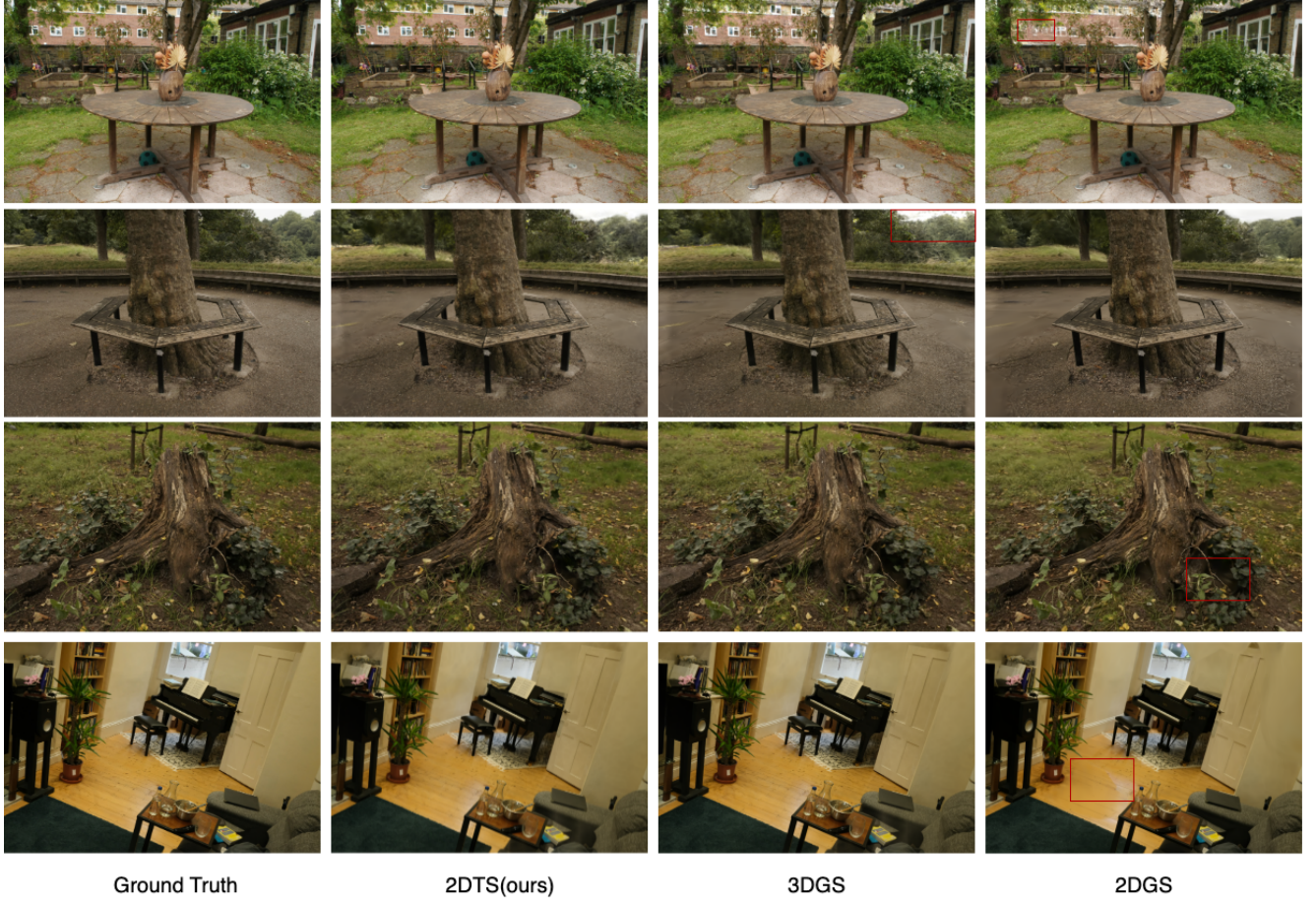


Figure 7. **Comparison between 2DTS, 3DGS, and 2DGS.** Visual comparison of our 2DTS method against 3DGS [17], and 2DGS [15] on the Mip-NeRF360 [2] dataset.

		chair	drums	ficus	hotdog	lego	materials	mic	ship	mean
PSNR	3DGS	35.71	25.94	34.60	37.42	36.04	30.08	35.69	30.61	33.26
	2DGS	35.22	26.03	35.38	37.39	35.77	29.98	35.76	30.40	33.24
	2DTS(Ours)	<b>35.83</b>	<b>26.19</b>	<b>35.92</b>	<b>37.57</b>	<b>35.92</b>	<b>29.88</b>	<b>35.65</b>	<b>30.72</b>	<b>33.46</b>
SSIM	3DGS	0.987	0.952	0.987	0.985	0.984	0.962	0.992	0.903	0.969
	2DGS	0.986	0.953	0.988	0.985	0.983	0.959	0.992	0.902	0.968
	2DTS(Ours)	<b>0.988</b>	<b>0.953</b>	<b>0.989</b>	<b>0.985</b>	<b>0.983</b>	<b>0.958</b>	<b>0.991</b>	<b>0.902</b>	<b>0.969</b>
LPIPS	3DGS	0.011	0.039	0.012	0.019	0.014	0.033	0.006	0.103	0.030
	2DGS	0.012	0.040	0.011	0.020	0.015	0.037	0.007	0.101	0.031
	2DTS(Ours)	<b>0.011</b>	<b>0.040</b>	<b>0.011</b>	<b>0.020</b>	<b>0.015</b>	<b>0.039</b>	<b>0.007</b>	<b>0.102</b>	<b>0.031</b>

Table 4. PSNR  $\uparrow$ , SSIM  $\uparrow$ , LIPPS  $\downarrow$  scores for NeRF-Synthetic [24] dataset.

		Truck	Train	Dr Johnson	Playroom
PSNR	3DGS	25.59	<b>22.33</b>	29.32	30.40
	2DGS	25.34	21.84	29.39	<b>30.51</b>
	2DTS(Ours)	<b>25.74</b>	21.99	<b>29.47</b>	30.30
SSIM	3DGS	0.889	0.821	0.899	<b>0.909</b>
	2DGS	0.882	0.811	0.901	0.908
	2DTS(Ours)	<b>0.898</b>	<b>0.839</b>	<b>0.903</b>	0.906
LPIPS	3DGS	<b>0.129</b>	<b>0.191</b>	<b>0.235</b>	<b>0.229</b>
	2DGS	0.146	0.213	0.243	0.241
	2DTS(Ours)	0.180	0.237	0.239	0.245

Table 5. PSNR  $\uparrow$ , SSIM  $\uparrow$ , LIPPS  $\downarrow$  scores for Tanks & Temples [18] and Deep Blending [13] dataset.

		chair	drums	ficus	hotdog	lego	materials	mic	ship	mean
PSNR	2DGS-Mesh	25.43	20.29	18.52	26.09	23.42	18.93	22.45	21.77	22.11
	Nvdiffire-Mesh	<b>31.60</b>	24.10	<b>30.88</b>	<b>33.04</b>	29.14	<b>26.74</b>	<b>30.78</b>	26.12	<b>29.05</b>
	2DTS-Mesh (Ours)	31.00	<b>24.26</b>	29.00	32.02	<b>32.86</b>	24.13	30.19	<b>26.89</b>	28.79
SSIM	2DGS-Mesh	0.899	0.849	0.884	0.922	0.871	0.855	0.914	0.771	0.871
	Nvdiffire-Mesh	0.969	0.916	<b>0.970</b>	<b>0.973</b>	0.949	<b>0.923</b>	<b>0.977</b>	0.833	0.939
	2DTS-Mesh (Ours)	<b>0.969</b>	<b>0.937</b>	0.965	0.971	<b>0.970</b>	0.907	0.976	<b>0.868</b>	<b>0.945</b>
LPIPS	2DGS-Mesh	0.092	0.154	0.119	0.097	0.123	0.128	0.082	0.245	0.130
	Nvdiffire-Mesh	0.045	0.101	<b>0.048</b>	<b>0.060</b>	0.061	<b>0.100</b>	<b>0.040</b>	0.191	0.081
	2DTS-Mesh (Ours)	<b>0.039</b>	<b>0.078</b>	0.052	0.071	<b>0.040</b>	0.133	0.046	<b>0.172</b>	<b>0.077</b>
CD(1e-3)	2DGS-Mesh	96.8	56.1	509.1	55.1	12.7	<b>9.7</b>	26.1	<b>167.5</b>	116.7
	Nvdiffire-Mesh	57.4	32.5	<b>15.4</b>	27.2	26.7	18.0	<b>9.8</b>	393.0	72.5
	2DTS-Mesh (Ours)	<b>39.3</b>	<b>22.3</b>	22.0	<b>20.2</b>	<b>6.7</b>	12.2	25.9	267.0	<b>51.9</b>
Count(K)	2DGS-Mesh	415	532	146	445	763	472	274	1547	574
	Nvdiffire-Mesh	102	<b>65</b>	39	57	111	<b>58</b>	<b>22</b>	190	81
	2DTS-Mesh (Ours)	<b>80</b>	72	<b>33</b>	<b>49</b>	<b>97</b>	64	68	<b>80</b>	<b>68</b>

Table 6. PSNR  $\uparrow$ , SSIM  $\uparrow$ , LIPPS  $\downarrow$  and Chamfer Distance (CD)  $\downarrow$  scores for Nerf-synthetic [24] dataset. Face counts of the meshes are also reported.

### B.3. Mesh Extraction on Large Scenes

Figure 8 shows the qualitative comparison of our method with 2DGS and 3DGS method on the MatrixCity [21] dataset. The experiments are described in the *Mesh Extraction on Large Scenes* section of the main paper.



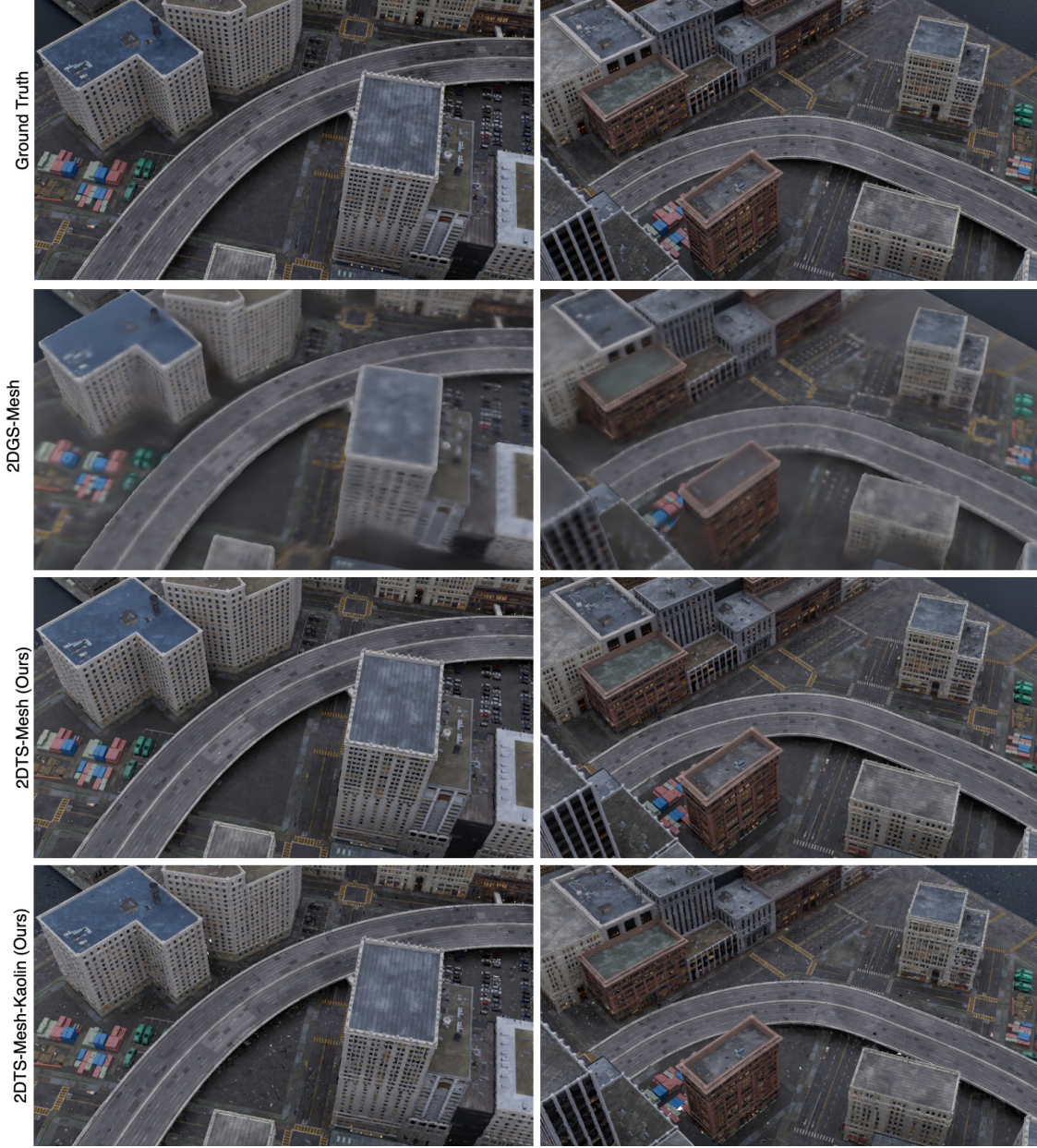


Figure 8. **Comparison of Mesh Extraction.** Visual comparison of our method with 2DGS [15] on the MatrixCity [21] dataset. The 2DGS results are rendered by the Kaolin renderer. For our method, we provide the results rendered by both our custom renderer and the Kaolin renderer.